

Document downloaded from:

<http://hdl.handle.net/10251/176992>

This paper must be cited as:

Alcántara-Ávila, F.; Gandía-Barberá, S.; Hoyas, S. (2019). Evidences of persisting thermal structures in Couette flows. *International Journal of Heat and Fluid Flow*. 76:287-295.
<https://doi.org/10.1016/j.ijheatfluidflow.2019.03.001>



The final publication is available at

<https://doi.org/10.1016/j.ijheatfluidflow.2019.03.001>

Copyright Elsevier

Additional Information

Evidences of persisting thermal structures in Couette flows

Francisco Alcántara-Ávila^a, Sergio Gandía-Barberá^a, Sergio Hoyas^{a,*}

^a*Instituto Universitario de Matemática Pura y Aplicada, Universitat Politècnica de València, Valencia 46022, Spain.*

Abstract

DNS of passive thermal turbulent Couette flow at several friction Reynolds numbers (180, 250, and 500), and the Prandtl number of air are presented. The time averaged thermal flow shows the existence of long and wide thermal structures never described before in Couette flows. These thermal structures, named CTFS (Couette Thermal Flow Superstructures), are defined as coherent regions of hot and cold temperature fluctuations. They are intrinsically linked to the velocity structures present in Couette flows. Two different 2D symmetries can be recognized, which get stronger with the Reynolds number. These structures do not affect the mean flow or mean quantities as the Nusselt number. However, turbulent intensities and thermal fluxes depend on the width of the structures, mainly far from the walls. Since the width of the structures is related to the channel width, the statistics of thermal Couette flow are to some point box-dependent.

1. Introduction

Wall turbulence is probably one of the open problems in physics with more applications in daily life. Due to the highly non-linear behaviour of

*Corresponding author. e-mail: serhocal@mot.upv.es. Tel: +34 - 96 38 77007 (ext 7663)
not submitted to Elsevier *July 4, 2019*

23 wall-turbulent flows, mainly basic research is restricted to simplified geome-
24 tries, as can be turbulent channel flows or boundary layers. In turbulent
25 channels, the fluid is confined between two parallel plates and the flow is
26 driven either by pressure, Poiseuille flows (PFs) [1, 2, 3, 4, 5], or shear, Cou-
27 ette flows (CFs) [6, 7, 8, 9]. Until very recently, CFs have been simulated
28 at a relatively small Reynolds number [6, 7, 9, 10, 11]. This is due to the
29 existence of very large-scale roll-like motions extending along the domain,
30 which were found experimentally [12, 13, 14]. In the later, Kitoh and Umeki
31 used an experimental apparatus with size 5120x27x880 *mm* with a lower wall
32 moving-belt. They performed several experiments at $Re = U_w h / \nu = 3750$,
33 where U_w was the half of the velocity of the moving-belt; h , the semi-height
34 of the channel; and ν , the kinematic viscosity; using a hot-wire probe to
35 measure flow statistics. In order to reduce the randomness of the appearance
36 of the structures in the experiment, they used a vortex generator in the core
37 region of the channel. The streamwise rolls that appeared downstream this
38 vortex generator became quasistationary without a noticeable decay. In or-
39 der to properly capture these rolls in numerical simulations, long and wide
40 computational boxes are needed, which makes simulations only available for
41 the largest supercomputers. In isothermal flows, these rolls are defined as co-
42 herent regions of either positive or negative streamwise velocity fluctuations.
43 They appear in pairs, creating a *structure* in the velocity field composed by
44 a couple of counter-rotating vortices aligned with the streamwise direction
45 [7, 15]. There is not a clear criterion to identify these structures. In ducts,
46 this structures has been identified using threshold functions [?], but this
47 has still to be done in Couette flows. They are mostly identified through

Work	Re_τ	L_x/π	L_z/π	Δx^+	Δy^+	Δz^+
	52			4.54	0.07 – 2.33	2.6
Tsukahara et al. [6]	126	14	4	11.03	0.18 – 5.67	6.31
	126	20	2	7.88	0.18 – 5.67	5.90
Avsarkisov et al. [7]	125 – 550	20	6	13	0.92 – 5.9	6.5
Pirozzoli et al. [8]	171 – 986	18	8	7	0.08 – 8.8	5
	93 – 501	100	5	10.25	0.040 – 6.33	5.13
Lee and Moser [9]	547	60	6	12.58	0.041 – 6.71	5.03
Kraheberger et al. [16]	250 – 1000	8	3	12.2	0.42 – 7.2	6.13
Gandía-Barberá et al. [10]	132	128	6	9.4	0.83 – 2.3	4.7
Komminaho et al. [11]	52	28	8	13.5	1.9 (mean)	7.7
Kawamura et al. [17]	180, 395	2	1	9.88	0.44 – 13	4.94
Debusschere and Rutland [18]	160	3.8	0.6	8.3	1.6	5
Tsukahara et al. [19]	52, 126	28.5	4	11.0	2.6 (mean)	6.3
Present work	180 – 500	16	6	8.4	0.83 – 2.3	4.3

Table 1: Parameters of previous CF simulations. Works in bold denotes that the thermal field has also been simulated. Third and fourth column show the maximum computational domain used in each work in x and z , respectively. Second column shows the ranges of Re_τ simulated at the corresponding computational boxes. Last three columns show the mesh resolution for each highest Re_τ case.

48 visualization employing some filtering [7, 9]. As it is shown later, there is
49 a clear organization of the velocity and thermal rolls in larger structures,
50 with two clear symmetries. As these rolls and structures have not received a
51 name, the generic term CTFS (Couette Thermal Flow Superstructure) will
52 be used to identify not only one particular velocity or thermal roll, but the
53 set composed by several of them.

54 Focusing in turbulent thermal flows, in a recent study for NASA, Slot-
55 nick et al. [20] highlighted the importance of thermal flows in aeronautical
56 applications in the foreseeable future. To cite another example, for Prandtl
57 numbers different to the one of air, a better knowledge of the dynamics of
58 thermal flows is needed for the simulation of nuclear Liquid Metal Reactors

59 (LMR) [21, 22]. Finally, heat transmission will be critical in the new trans-
60 portation system Hyperloop, as the flow between the pod and the pipe can
61 be thought as a CF. There exists a rich bibliography about the problem of
62 heat transfer in PFs, see [23, 24] and references therein. However, up to
63 the knowledge of the authors, only a few works address the problem of heat
64 transfer for CFs [18, 17, 19]. These works were a challenge in their times,
65 but unfortunately in most of them, either the computational box used is too
66 narrow and short to properly describe the CTFS, or the Reynolds number
67 used is low. In fact, in the work of Debusschere and Rutland [18] it is ex-
68 plicitly stated that they are using a narrow box to remove the effects of the
69 velocity rolls. These authors affirm that these rolls are not probably present
70 in real-life devices. However, as it is said before, the rolls have been found
71 experimentally [12, 13, 14]. They are very long and could be even infinite
72 in length [9]. The rolls are also stable even to transversal flows [16] and
73 they affect the flow as secondary flows in ducts do [25]. Moreover, as it is
74 stated in this paper, CTFS do affect both the statistics of the flow and the
75 thermal field, as it is composed by rolls of both of fields. This appears to
76 be an effect of Couette boundary conditions. Table 1 shows the parameters
77 of previous CFs simulations, such as Re_τ , computational box size and mesh
78 resolution. In the case of a PF, Lozano-Durán and Jiménez for the flow field
79 [26], and Lluesma et al. for thermal flows [27], found out that relatively
80 small computational box of stream- and span-wise sizes of only $2\pi h \times \pi h$ can
81 satisfactorily recover the one-point statistics of the flow. The existence and
82 characterization of the CTFS, and its influence in the one-point statistics is
83 addressed for the first time in this work.

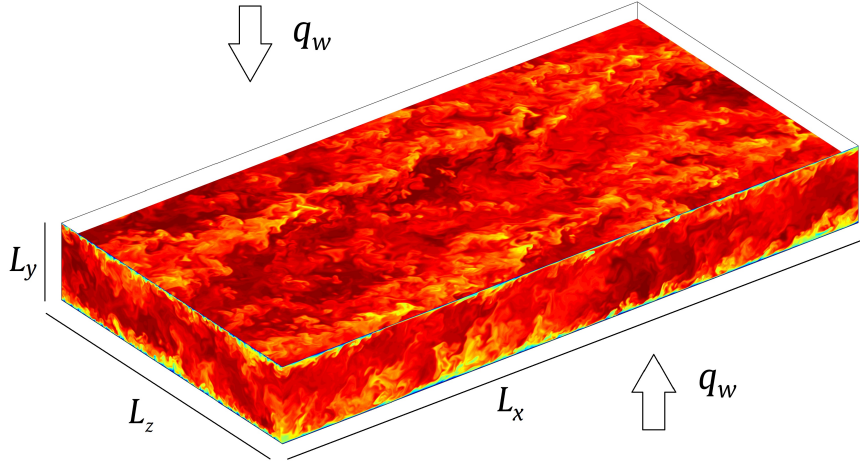


Figure 1: Thermal flow at $Re_\tau = 500$ for $Pr = 0.71$. The flow is driven by the shear of the top wall and moves from the left to the right. Both walls are considered isothermal, and the thermal heat flux, q_w , is constant.

84 The structure of the paper is as follows. In the second section, the numer-
 85 ical method is presented and validated. In the third section, the influence of
 86 the CTFS in the mean flow and in the one-point statistics is accounted and
 87 discussed. Finally, the fourth section contains the summary and conclusions.

88 2. Numerical setup

89 To perform this study, two DNS of a passive thermal flow in a Couette
 90 turbulent channel at $Re_\tau = 250$ and 500 , and $Pr = 0.71$ have been conducted
 91 within a computational box of $L_x = 16\pi h$, $L_y = 2h$ and $L_z = 6\pi h$, with pe-
 92 riodicity in the streamwise and spanwise directions. These are the cases V
 93 and VI in Table 2. A schematic representation of the computational box is
 94 shown in Figure 1, where the thermal field is plotted. Here, $Re_\tau = u_\tau h / \nu$ is
 95 the friction Reynolds number, Pr is the molecular Prandtl number, u_τ is the
 96 friction velocity, h is the semi-height of the channel and ν is the kinematic







Cases	Line	Re_τ	Re	Box	N_x	N_y	N_z	Tu_τ/h
I		166	3500	$4\pi h \times 0.5\pi h$	384	201	144	57.3
II		177	3500	$2\pi h \times \pi h$	192	201	192	79.9
III		176	3500	$4\pi h \times 2\pi h$	384	201	384	39.2
IV		178	3500	$16\pi h \times 6\pi h$	1536	251	1152	59.1
V		262	5400	$16\pi h \times 6\pi h$	1536	251	1152	88.9
VI		476	10500	$16\pi h \times 6\pi h$	3072	251	2304	58.1

Table 2: Parameters of the simulation. Friction and bulk Reynolds numbers are shown in columns three and four, respectively. The fifth column shows the box size of each case. N_x , N_y and N_z are the number of collocation points in each direction. The last column contains the time spent to compile statistics in terms of eddy turnovers. The lines used through the paper to identify the different cases are shown in the second column.

viscosity. In addition, four CF simulations with different size of boxes in x and z dimensions ($4\pi h \times 0.5\pi h$, $2\pi h \times \pi h$, $4\pi h \times 2\pi h$ and $16\pi h \times 6\pi h$) were also conducted at $Re_\tau = 180$ and the Prandtl number of air (cases I-IV in Table 2). These simulations were performed to check whether or not the size of the box has an influence in the rolls and, consequently, in the mean and one-point statistics. The superscript (+) indicates that the quantities have been normalized either by u_τ or by the friction temperature θ_τ . The streamwise, wall-normal, and spanwise coordinates are x , y , and z . The corresponding velocity components are U , V and W or, using index notation, U_i . Defining the average operator $\langle \cdot \rangle_{x_i}$ as

$$\langle \phi \rangle_{x_i} = \frac{1}{L_{x_i}(t_1 - t_0)} \int_{t_0}^{t_1} \int_0^{L_{x_i}} \phi dx_i dt, \quad (1)$$

the value of $\langle \phi \rangle_x$ can be thought as the mean in x of the time-averaged field ϕ . Statistically averaged quantities in x and z are denoted by an overbar, $\bar{\phi} = \langle \phi \rangle_{xz}$, whereas fluctuating quantities are denoted by lowercase letters, i. e., $U = \langle U \rangle_{xz} + u = \bar{U} + u$.

112 The temperature is simulated as a passive scalar and denoted by T . The
 113 transformed temperature is Θ , which is defined as $\Theta = T - T_w$, where T_w
 114 is the temperature at the wall. In the streamwise direction, it is assumed
 115 that temperature increases linearly. Subtracting T_w to T makes Θ periodic,
 116 as T_w carries the non-periodic part of the thermal flow. These conditions
 117 are known as Mixed Boundary Conditions (MBC) [28]. Among other things,
 118 MBC allow the use of highly efficient Fourier methods in the streamwise
 119 direction.

120 The flow can be described by means of the momentum and mass balance
 121 equations, as well as the energy conservation principle. These equations are
 122 later solved using the LISO code, which has successfully been employed to run
 123 some of the largest simulations of turbulence [2, 7, 10, 24, 27, 29, 30]. Briefly,
 124 the code uses the same strategy than [1], but using a seven-point compact
 125 finite differences in the wall-normal direction with fourth-order consistency
 126 and extended spectral-like resolution [31]. The temporal discretization is a
 127 third-order semi-implicit Runge-Kutta scheme [32]. The wall-normal grid
 128 spacing is adjusted to keep the resolution at $\Delta y = 1.5\eta$, i.e., approximately
 129 constant in terms of the local isotropic Kolmogorov scale $\eta = (\nu^3/\epsilon)^{1/4}$.
 130 In wall units, Δy^+ varies from 0.83 at the wall, up to $\Delta y^+ \simeq 2.3$ at the
 131 centerline. The wall-parallel resolution in physical space for x and z is $\Delta x^+ \simeq$
 132 8.4 and $\Delta z^+ \simeq 4.3$.

133 In every simulation, the flow had to evolve from an initial file, which
 134 has been taken from previous different simulations. The code was run until
 135 the transition phase had passed and the flow had adjusted to the new set
 136 of parameters. Once the flow is in a statistically steady state, statistics are

137 compiled. The running times used to compile statistics are shown in the
 138 rightmost column of Table 2. They are given in terms of eddy-turnovers.
 139 The transitions before the simulations reached a statistically steady state,
 140 which can be very time consuming, are not contemplated in this table.

141 In order to further validate the database, two procedures have been fol-
 142 lowed. First, the total shear stress equation, which in CFs is

$$143 \quad 1 + \frac{d\bar{U}}{dy} + \overline{uv} = 0, \quad (2)$$

144 is used to validate the isothermal flow. Second, the total heat flux is calcu-
 145 lated and compared with the molecular and turbulent heat flux. The flux
 146 conservation equation is given by [24]

$$147 \quad \overbrace{\Theta_\tau^s - \frac{1}{Re_\tau} \int_0^{y^+} \frac{U_1^+}{\langle U^+ \rangle_{xyz}} dy}^{\text{Total}} = \overbrace{\frac{1}{Pr} \frac{d\Theta^+}{dy^+}}^{\text{Molecular}} \overbrace{- \frac{v^+ \theta^+}{}}^{\text{Turbulent}}, \quad (3)$$

148 where $\Theta_\tau^s = \partial_y \Theta|_{y=0} / (Re_\tau Pr)$ is the friction temperature at the stationary
 149 wall.

150 The results of this validation are shown in Figure 2, for cases V and VI.
 151 In Figure 2a, apart from the small error, a very good agreement is found
 152 between both simulations, as the curves collapse almost perfectly. Molecular
 153 and turbulent heat fluxes are compared with the total flux in Figure 2b.
 154 The total error is defined as the difference between the RHS and the LHS
 155 of Equation 3. It has been considered that enough statistics were obtained
 156 when this error was below 10^{-3} .

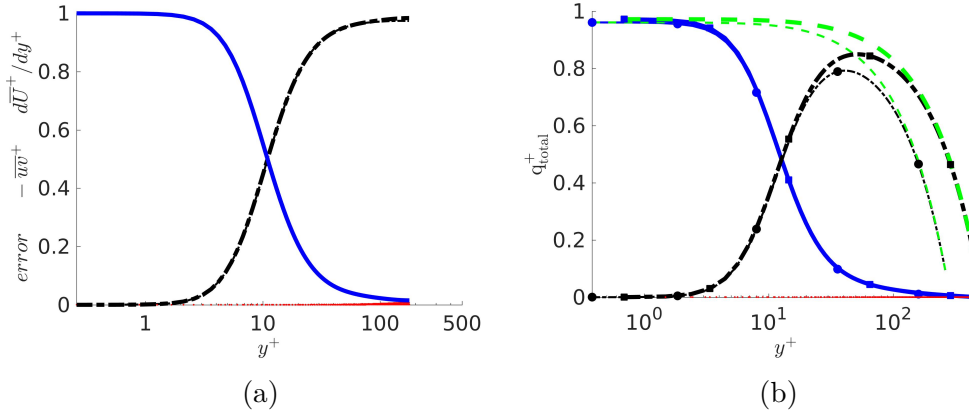


Figure 2: Colour online. For $Re_\tau = 250$ (thin lines) and 500 (thick lines). (a) Shear stress: $d\bar{U}^+/dy^+$ (blue, solid), \overline{w}^+ (black, dash-dot) (b) Heat fluxes: Molecular (blue, solid), turbulent (black, dash-dot) and total (green, dash). In both cases, the red pointed line represents the difference between LHS and RHS of either Equation 2 or 3.

157 3. Results and discussion

158 CFs and PFs affect in different ways the thermal flow under MBC for these
 159 low Reynolds numbers. A first result is that mean and one-point statistics are
 160 no longer symmetric. In Figure 3a, it can be seen that temperature profiles
 161 are slightly different in both halves of the channel for CFs. On the other
 162 hand, the PF thermal profile is perfectly symmetric [27]. A first insight of
 163 the collapse of the statistics depending on the computational box size can be
 164 obtained from Figure 3b. Here, temperature profiles of the bottom part of the
 165 channel of cases I-IV are shown. All profiles of $\bar{\Theta}^+$ collapse fairly well, except
 166 for case I. This case uses a computational box similar to the one in [18]. The
 167 collapse error is probably due to the narrowness of the box [27]. Another
 168 remarkable difference between CFs and PFs is the presence or absence of a
 169 thermal logarithmic layer between the viscous and the outer layers. For PFs,
 170 this logarithmic layer appears for $Pr \approx 0.3$ and above [24]. However, for CFs,

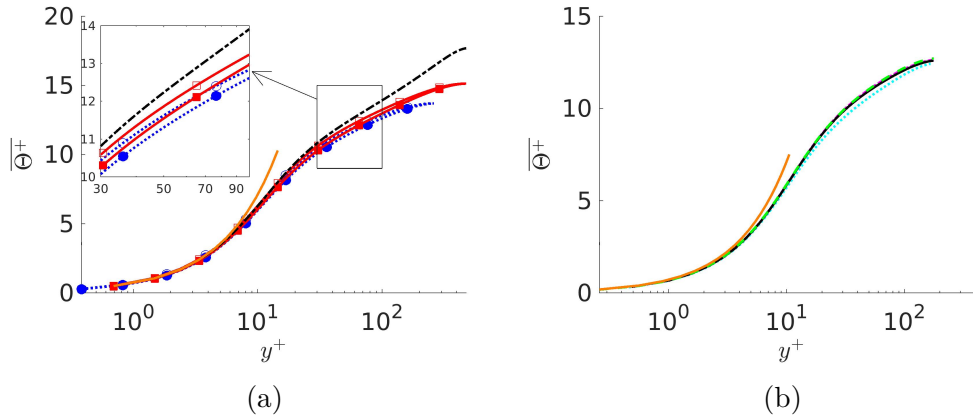


Figure 3: Colour online. (a) $\bar{\Theta}^+$ for cases V (blue dashed) and VI (red solid). Closed symbols, bottom half. Empty symbols, top half. Black dash-pointed line represents a PF at $Re_\tau = 497$. (b) $\bar{\Theta}^+$ for cases I-IV at the stationary wall. In both cases, orange solid line: thermal law of the wall, $\bar{\Theta}^+ = Pr \cdot y^+$. Colours as in Table 2.

171 it is not present for $Pr = 0.71$. It is uncertain if this logarithmic layer in the
 172 temperature field will appear for higher Prandtl numbers in a CF. However,
 173 as it is said before, CFs are far more computationally expensive than PFs.
 174 To see if a thermal logarithmic layer does exist in CFs will still be a challenge
 175 for the next decade.

176 In Figure 4 turbulent intensities for the three different Reynolds numbers
 177 are shown. As a general result, it is seen that the maximum of all turbu-
 178 lent intensities increases and moves towards the wall with an increase of the
 179 Reynolds number. A difference between CFs and PFs appears in u'^+ , Figure
 180 4a. A second maximum can be observed for the higher Reynolds number,
 181 500. This was already noted in previous simulations [7]. and from this work
 182 it is confirmed that for $Re_\tau = 500$, u'^+ shows a second maximum in the
 183 central region of the channel. Also, as it was shown before for $\bar{\Theta}^+$, intensities
 184 related with temperature are not totally symmetric or antisymmetric. This

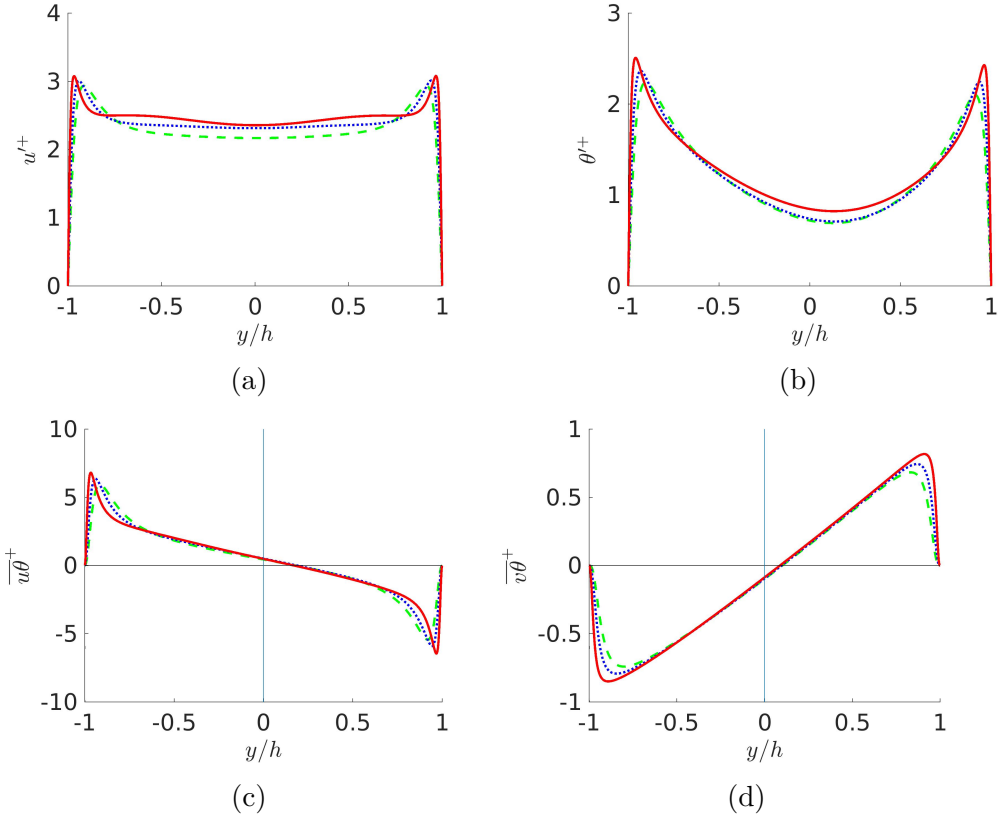


Figure 4: Colour online. (a) u'^+ , (b) θ'^+ , (c) $\overline{u\theta}$ and (d) $\overline{v\theta}$ for cases IV-VI. Colours as in Table 2.

185 can be seen in Figures 4b, 4c and 4d. Another important point is the anti-
 186 symmetry obtained for the turbulent intensity $\overline{u\theta}$, Figure 4c. This opposes
 187 to the behaviour of $\overline{u\theta}$ in a PF when the MBC is employed, where a symmetric
 188 profile is obtained. This is discussed below.

189 A distinctive feature of CFs is the existence of velocity large instantaneous
 190 structures in the flow [10, 11]. Corresponding long and wide structures of
 191 the thermal fluctuation field are also present. These instantaneous struc-
 192 tures, Figure 5, appear in a strip-like pattern in $x - z$ planes. Isocontours

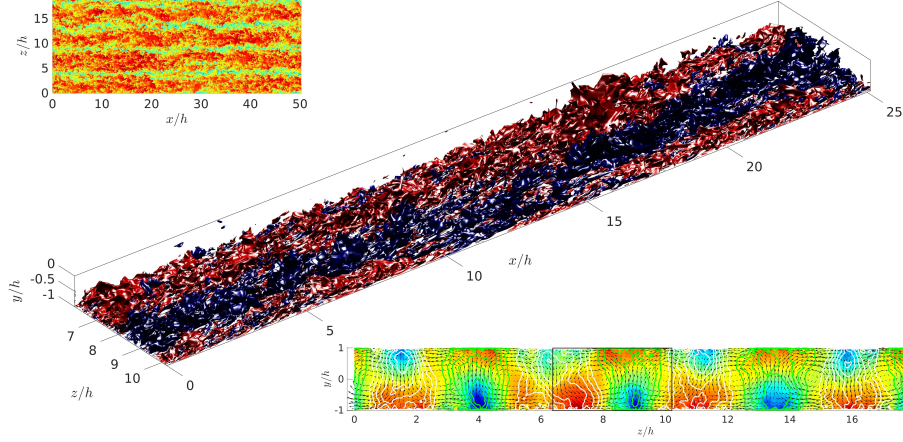


Figure 5: Instantaneous value of θ at $Re_\tau = 500$. Top: $x - z$ -plane at $y = 0.3h$. Middle: isocontours of θ . Red, hotter than mean; blue, colder than mean. Bottom: mean in the streamwise direction of u (isolines), v and w (arrows) and θ (contours). The black box indicates the region plotted in the middle figure.

193 of θ , 5 middle, show long and wide, coherent three dimensional thermal
 194 structures, that mainly extend along the streamwise direction. CTFS are a
 195 consequence of this particular distribution of the values of \vec{u} and θ , as they
 196 reflect the effect of these instantaneous structures in the time-averaged flow
 197 and thermal field. CTFS are defined as a characteristic of the time-averaged
 198 perturbations, which does not need to be zero. A first proof of the existence
 199 of the CTFS appears in the x -averaged fields. The values of $\langle u \rangle_x$, $\langle v \rangle_x$,
 200 $\langle w \rangle_x$, and $\langle \theta \rangle_x$ are shown in Figure 6b. In this figure, white and green lines
 201 represent contours of positive and negative $\langle u \rangle_x$, respectively. $(\langle v \rangle_x, \langle w \rangle_x)$
 202 vector field is represented by arrows. Colours show contours of $\langle \theta \rangle_x$. While
 203 the U -velocity structures expand across the whole height of the channel, a
 204 pair of hot-cold thermal structures appear for every velocity structure. These

205 thermal structures are as long as the box itself, $L_x = 16\pi h$ (Figure 6c), in
 206 the same way as the velocity structures [9].

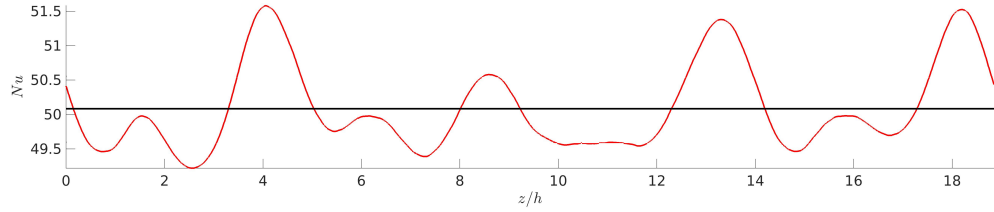
207 The black box of Figure 6b shows the footprint of a CTFS. These struc-
 208 tures are made of two velocity rolls (positive-negative velocity fluctuations)
 209 and four thermal ones. They are organized in such a way that the thermal
 210 flux, $\overline{u\theta}$, is positive in the lowest part of the channel and negative in the top
 211 one. A large vortex in $\langle v \rangle$ and $\langle w \rangle$ appears at the center of the CTFS.

212 In PFs, these structures do not exist. In fact, the time averaged of any
 213 perturbation field is simply noise. This is due to the inclination of large-scale
 214 structures in the PF. In this context, Abe et al. [33] recently examined the
 215 effects of the streamwise domain size in the PF for a flow field for $Re_\tau = 395$
 216 and 1020. They found out that when the streamwise domain is reduced to
 217 $L_x^+ \approx 400$ for $Re_\tau = 1020$, the two-dimensional behavior is indeed established
 218 in the PF. Thus, only trivial symmetries are present. CTFS, on the other
 219 hand, exhibit two non-trivial symmetries never described before. First, there
 220 is a translation symmetry of period $2L_R$. This length is the distance between
 221 the centers of two consecutive rolls. In this case is $L_R/h = 6\pi/8 \approx 2.3$.
 222 Second, there exists a symmetry, for $\langle \theta \rangle_x$, with respect to the origin of every
 223 (v, w) vortex (see black box of Figure 6b).

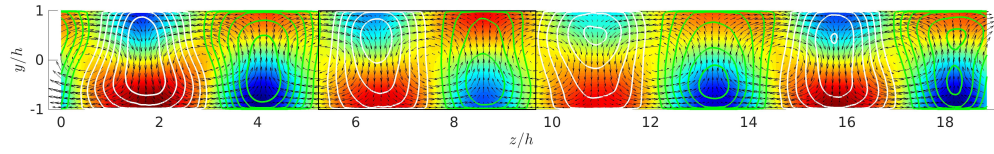
224 Quantities related to the mean flow seem not to be seriously affected
 225 by the CTFS. As an example, the most important parameter for modeling
 226 thermal boundary layers, the Nusselt number, has been computed as in[34],

$$227 \quad Nu = \frac{Lh}{\kappa} = \frac{2Re_\tau Pr}{\langle \Theta^+ \rangle_m} = \frac{2Pe_\tau}{\langle \Theta^+ \rangle_m}, \quad (4)$$

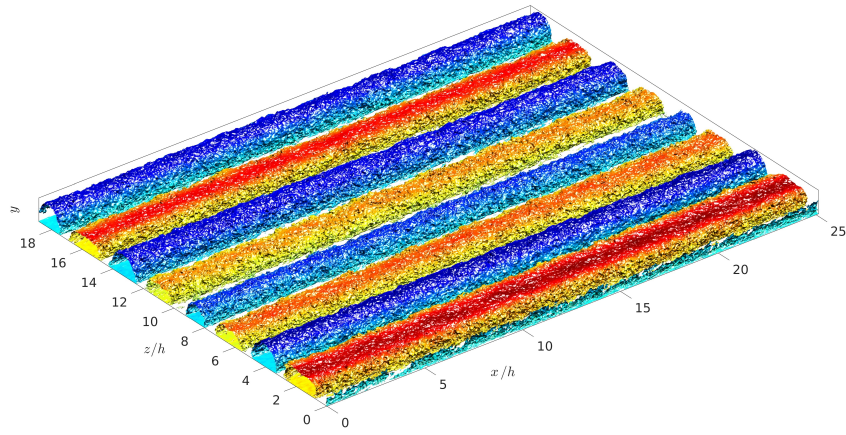
228 where L is a characteristic length, in this case it is the channel height of the



(a)



(b)



(c)

Figure 6: Colour online. Case VI. (a) Local Nusselt number averaged in x direction (red) and averaged Nusselt number (black). (b) Contours of $\langle \theta \rangle_x$. White and green lines represent contours of positive and negative $\langle u \rangle_x$, respectively. $(\langle v \rangle_x, \langle w \rangle_x)$ vector field is represented by arrows. (c) Isocontours of cold (blue) and hot (red) $\langle \theta \rangle$. The values of the isocontours are $0.4 \langle \theta \rangle_{min}$ and $0.4 \langle \theta \rangle_{max}$ for the cold and hot $\langle \theta \rangle$, respectively.

229 computational box, $2h$; \mathfrak{h} is the convective heat transfer coefficient; κ is the
 230 thermal conductivity; and $\langle \overline{\Theta^+} \rangle_m$ is the mixed mean transformed tempera-
 231 ture, defined as [34]

$$232 \quad \langle \overline{\Theta^+} \rangle_m = \int_0^1 \overline{U^+ \Theta^+} dy / \int_0^1 \overline{U^+} dy \quad (5)$$

233 Table 3 summarizes the difference in Nusselt number for CFs and PFs.
 234 Values of Nu_P at $Re_\tau = 180$ and 500 have been obtained from [34] and [24],
 235 respectively. In order to obtain Nu_P at $Re_\tau = 250$ a new simulation was run
 236 by the authors and then Nu_P was computed using (5).

237 One can consider the hypothesis of a linear behaviour of the Nusselt
 238 number in the range from $Re_\tau = 180$ to 500 . Therefore, precise values of
 239 Nu_P have been extrapolated to the Reynolds number of the corresponding
 240 CF. All simulations I-IV give approximately the same value (less than a
 241 0.6% deviation) of Nu_C , regardless of the box size. Thus, short and narrow
 242 boxes do not introduce a big error when calculating the Nusselt number. An
 243 interesting property to be investigated is the difference in Nu between CFs
 244 and PFs. As can be seen in Table 3, this difference gets reduced with an
 245 increase of Re_τ .

Re_τ	Nu_C	Nu_P	Δ (%)
178	21.60	18.33	17.9
262	29.39	25.35	16.0
476	47.96	42.86	11.9

Table 3: Nu for each Reynolds in a CF, second column, and a PF, third column. The fourth column shows the relative difference.

246 However, local Nusselt number can be different to the average one due
 247 to the effect of the CTFS. In Figure 6a local Nusselt number for Case VI is

248 shown in red and the averaged one, in black. Despite it looks like hot rolls
 249 compensate the cold ones when averaging in the y direction (Figure 6b), local
 250 Nusselt number shows that the lower thermal rolls are stronger, especially
 251 the cold ones. For this reason, $\langle Nu \rangle_x$ have greater peaks above the average
 252 Nu in the z coordinates where a cold roll is present in the lower part of
 253 the channel. Here, local Nu number differs up to a 3% from the averaged
 254 one. Remark that local Nusselt number shows two frequencies: one that
 255 corresponds to the wavelength of the CTFS. The other, whose amplitude is
 256 half of the CTFS one and whose intensity is lower, corresponds to smaller
 257 structures that cannot be seen in isocontours plots of mean u'^+ and θ'^+ , but
 258 that will be observed in the spectral analysis.

259 To conclude the analysis of the Nusselt number, a comparisson of the re-
 260 sults obtained in this work with the correlation obtained by Abe and Antonia
 261 in [35] for PFs has been performed. This correlation expresses the Nusselt
 262 number as a function of Reynolds bulk number, Re_b , where the entire height
 263 of the channel is considered for its calculation,

$$264 \quad Nu = h_t Re_b Pr, \quad (6)$$

265 where h_t is the heat transfer coefficient, computed as

$$266 \quad h_t = \frac{\sqrt{\frac{C_f}{2}}}{2.18 \ln \left(Re_b \frac{\sqrt{C_f}}{2\sqrt{2}} \right) + 2.4}, \quad (7)$$

267 where C_f is the skin friction coefficient, which is obtained form the next
 268 expression,

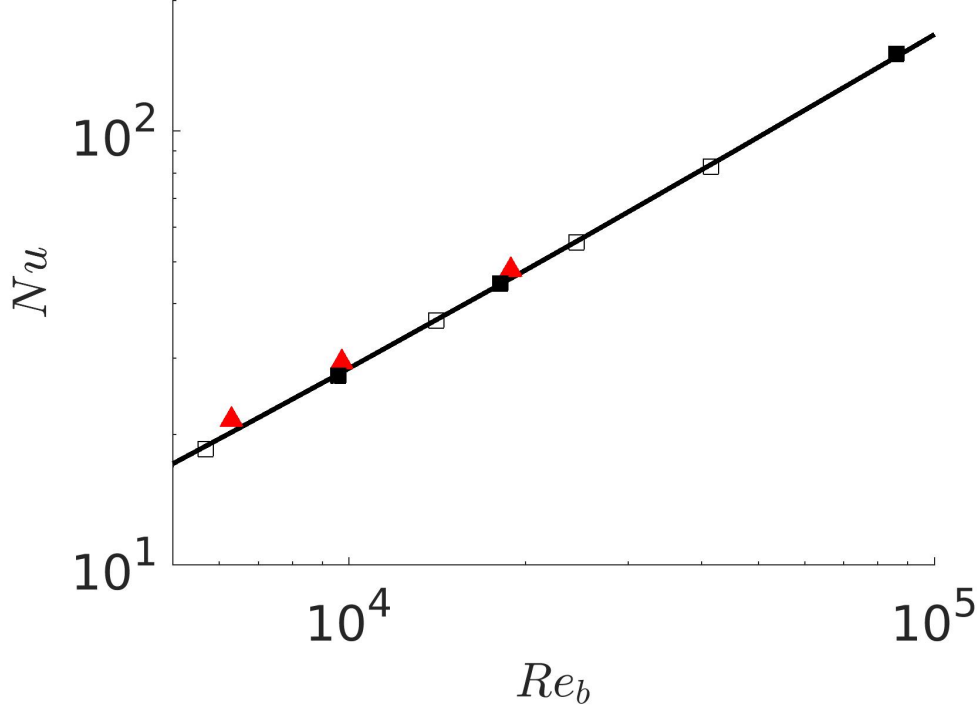


Figure 7: Colour online. Nusselt number as a function of Re_b for Prandtl number of 0.71. Black line represents correlation of Abe and Antonia [35]. \blacktriangle represent Nu for CFs, \square are the Nu values for PFs from [35] and \blacksquare are the Nu values for PFs from [24].

$$\frac{1}{C_f} = 1.8 \ln (Re_b \sqrt{C_f}) - 0.163. \quad (8)$$

Figure 7 represents the values of the Nusselt numbers obtained for the CFs, \blacktriangle , and the ones obtained for PFs in [35], \square , and [24], \blacksquare . As it was expected, Nu for CFs are slightly above the line of the correlation for PFs and when Re_b is increased, this difference gets reduced.

A quadrant analysis for case VI, like in [36] for a PF, has been performed to see if the large-scale temperature structures are active in generating wall-normal turbulent heat flux. Also, the generation mechanism of $\overline{v\theta^+}$ is com-

277 pared with the one of \overline{uv}^+ and $\overline{u\theta}^+$. For this analysis, the flux is divided in
 278 four quadrants. In the case of the wall-normal heat flux, quadrant 1 ($v > 0$
 279 and $\theta > 0$) and quadrant 3 ($v < 0$ and $\theta < 0$), are referred to as the outward
 280 and inward interactions. While quadrant 2 ($v > 0$ and $\theta < 0$) and quadrant
 281 4 ($v < 0$ and $\theta > 0$) are referred to as the ejection and sweep events. In
 282 Figure 8 all three fluxes are plotted together with the decomposition in the
 283 four quadrants. In contrast with the results obtained in [36], the generation
 284 mechanism of \overline{uv}^+ and $\overline{v\theta}^+$ are quite different in a CF. On the other hand,
 285 $\overline{u\theta}^+$ and $\overline{v\theta}^+$ generation mechanisms are very similar, although interactions
 286 and events occur in the opposite walls: for $\overline{u\theta}^+$, outward and inward interac-
 287 tions occur in the stationary wall, while for $\overline{v\theta}^+$, ejection and sweep events
 288 happen in this wall. The opposite happens in the moving wall. This is per-
 289 fectly correlated with the result obtained in the black box of Figure 6b, i.e.
 290 the CTFS. In the black box can be seen how, in the lower part of the channel,
 291 hot θ' are related with positive u' (quadrant 1) and negative v' (quadrant 4)
 292 or cold θ' are related with negative u' (quadrant 3) and positive v' (quadrant
 293 2). The contrary occurs in the upper part of the channel.

294 A spectral analysis has been performed for u^+ and θ^+ . In Figure 9, 1D
 295 spectral density of the two intensities is shown for $Re_\tau = 250$ and 500, for
 296 coordinates x and z and a wall distance of $y^+ = 160$. The most important
 297 result is the peak that appears in Figure 9b at $\lambda_z^+ \approx 4.7$, which agrees with
 298 the one obtained in [37]. The wavelength of the peak corresponds to the
 299 width of the CTFS or, in other words, to half of the width of the velocity and
 300 thermal fluctuation structures shown previously in Figure 6b, i.e. $2L_R \approx 4.7$.
 301 In addition, it can be appreciated that the peak increases as the Reynolds

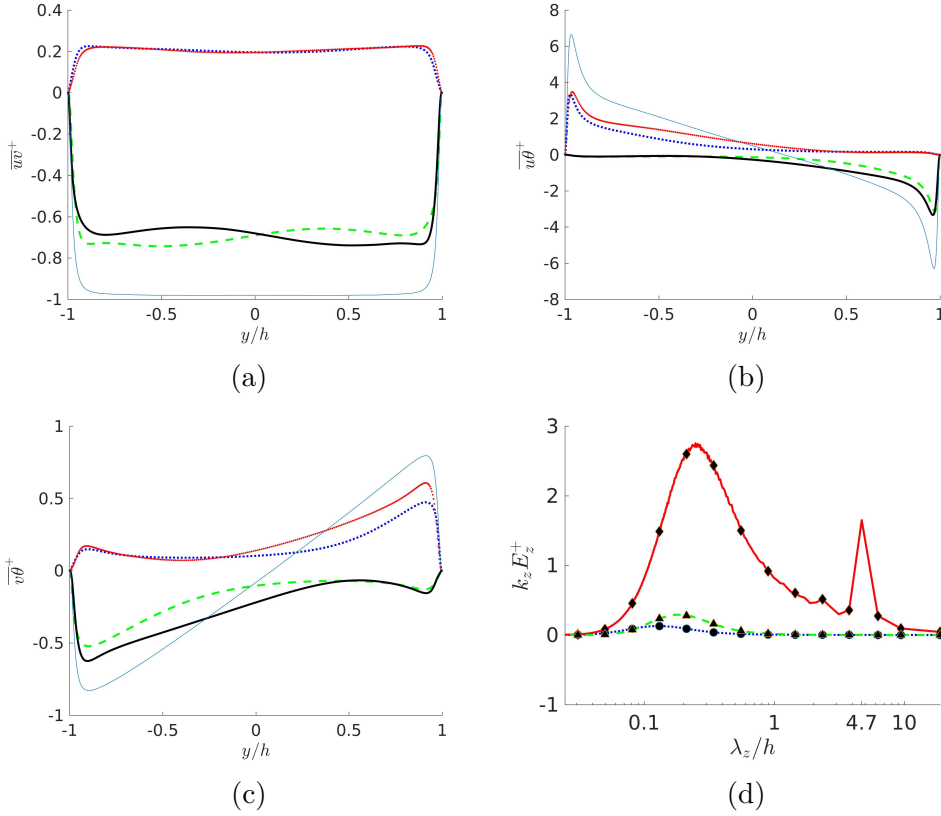


Figure 8: Colour online. Quadrant analysis of case VI for a) $\overline{uv^+}$, b) $\overline{u\theta^+}$ and c) $\overline{v\theta^+}$. Dotted blue line: quadrant 1; dashed green line: quadrant 2; solid red line: quadrant 3; solid black line: quadrant 4. Solid thin blue line is the sum of the four quadrants. d) 1D coespectral density of u^+ , θ^+ and $\overline{u\theta^+}$ (red solid).

302 number increases, which means that the structures become more intense for
 303 higher Reynolds numbers.

304 Contour plots are shown in Figure 10 to visualize the y dependences of
 305 the spectrum. First, mention that at $y^+ = 10$ there is a concentration of
 306 energy corresponding to the small scales of the velocity and temperature,
 307 intrinsic to every turbulent flow. The new feature appears at the previously
 308 mentioned wavelength, $\lambda_z^+ \approx 4.7$, which corresponds to the CTFS. Here it can

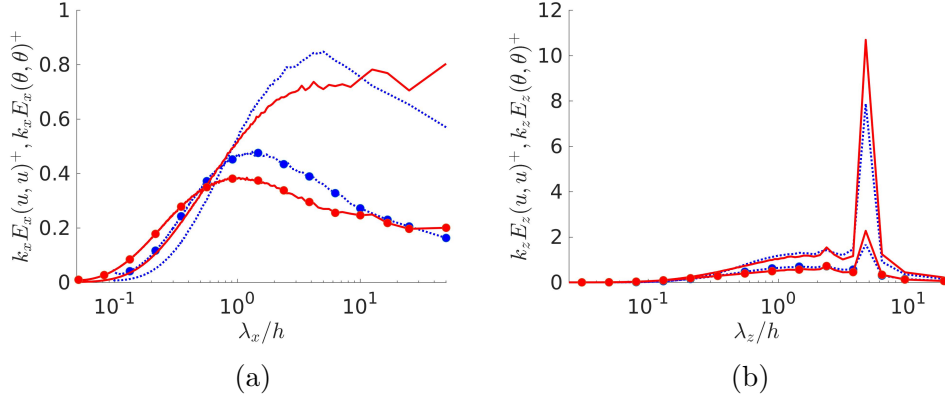


Figure 9: Colour online. 1D spectral density of u^+ (without marks) and θ^+ (●) at $Re_\tau = 250$ and 500 for (a) x and (b) z . $y^+ = 160$. Colours as in Table 2.

309 be seen how the velocity rolls are perfectly symmetric, while the temperature
 310 ones are more intense in the lower half of the channel. In addition, one can
 311 see a small increase of the energy intensity at $\lambda_z^+ \approx 2.3$, which is the half
 312 of the previously mentioned wavelength. This second harmonic is the one
 313 appreciated in the local Nusselt number, Figure 6a.

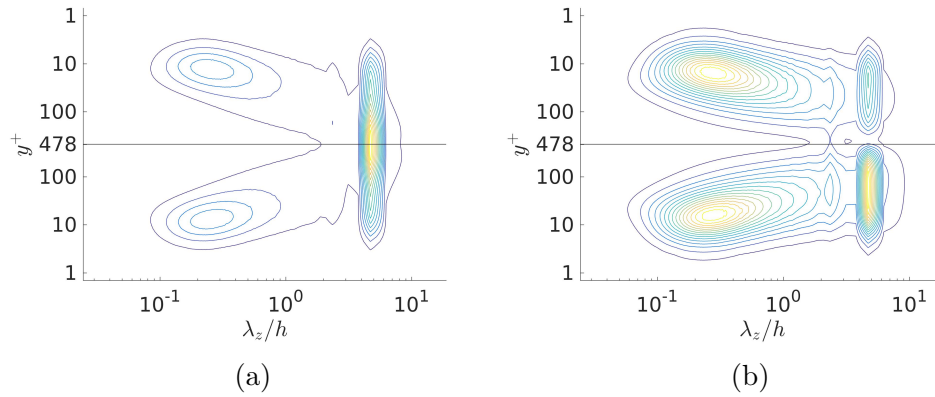


Figure 10: Colour online. Contours of a) u^+ and b) θ^+ spectral density for $Re_\tau = 500$ in the $Y - Z$ plane. Central horizontal line is the center of the channel. Vertical axis is the wall distance to the closest wall.

314 As it was said before in Figure 4c, one of the major differences between
315 PFs and CFs, when the same thermal boundary condition is used, is the
316 different behaviour of the streamwise thermal flux, $\overline{u\theta}$, shown in Figure 11c.
317 When the MBC is used, this flux is symmetric in the case of PFs and (almost)
318 antisymmetric for CFs. This antisymmetry is totally related to the second
319 symmetry of the rolls explained above. In the lower half of the channel,
320 hot temperature fluctuations are related to positive velocity fluctuations and
321 vice-versa, causing a positive value of $\overline{u\theta}$. This situation is inverted in the
322 upper part, where hot temperature fluctuations appear with negative velocity
323 fluctuations, causing a negative value of $\overline{u\theta}$. Other point of view to explain
324 the antisymmetry of $\overline{u\theta}$ is the difference in the flow and thermal boundary
325 conditions. In a CF, the flow boundary conditions is that one wall is moving,
326 while other wall is stationary. This is analogous to a temperature difference
327 for the thermal boundary condition. However, in the present work, the MBC
328 is used for the thermal field. Therefore, both walls are kept at the same
329 temperature, which is analogous to a Poiseuille boundary condition for the
330 velocity field.

331 All intensities related with temperature (Figures 11b, 11c, and 11d) are
332 almost symmetric or antisymmetric, in contrast with PFs, where perfect
333 symmetry or antisymmetry is always present in both halves of the channel.
334 Values of θ^+ have been compared with other trusted simulations for PFs [34]
335 and pipe flows [38] and tendencies agree fairly well.

336 As it was shown before, the effect of the box size in the mean flow, both
337 in the mean temperature or the Nusselt number is small. This is not the
338 case for the statistics of the perturbations. As it can be seen in Figure 11,

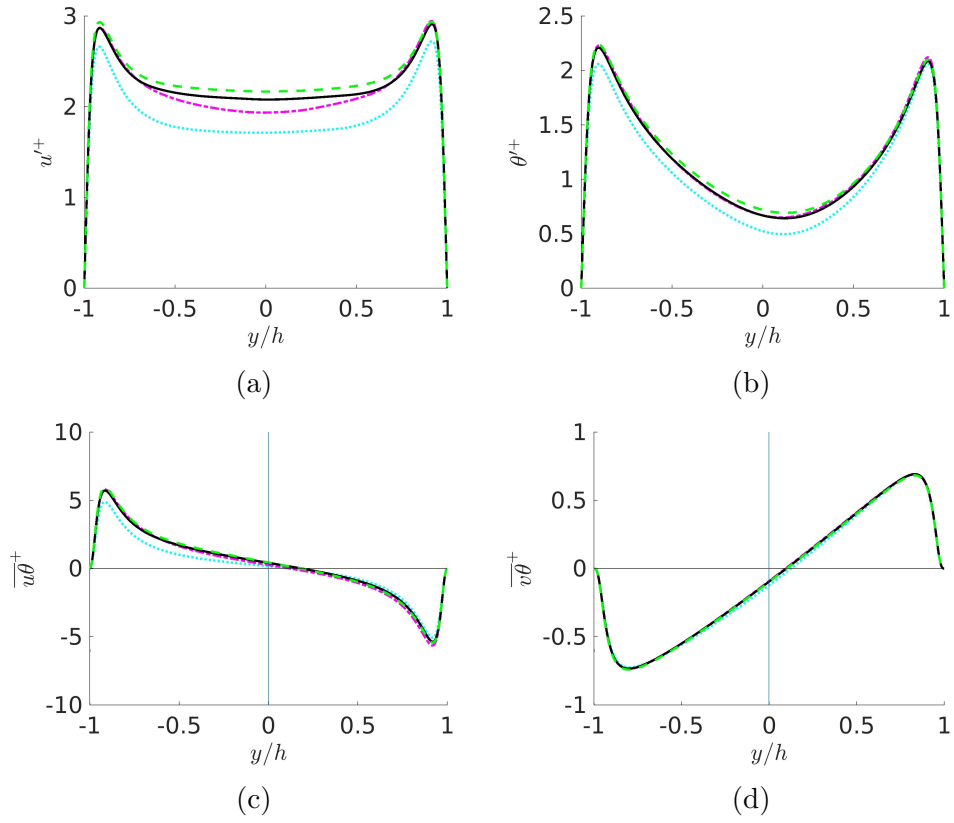


Figure 11: Colour online. (a) u'^+ , (b) θ'^+ , (c) $\overline{u'\theta'}$ and (d) $\overline{v'\theta'}$ for cases I-IV. Colours as in Table 2.

339 the one-point statistics of the flow for $Re_\tau = 180$ in different boxes do not
 340 collapse. The problem is evident in Figures 11a, 11b, and 11c, mainly for
 341 case I, but not only. However, in the case of PFs, a $(2\pi h, \pi h)$ box in x and
 342 z , respectively, is enough to accurately compute every first-order statistics
 343 [26, 27]. The collapsing problem here is also not an effect of the mesh size, as
 344 the cell lengths used for cases I-IV are smaller than in many other available
 345 DNS.

346 Thus, the collapse problem has to be related to the CTFS. An analysis
 347 of θ in cases I-IV shows that the CTFS are always present (Figure 12), even
 348 if the box is too small (case I) to obtain accurate statistics [26, 27]. The
 349 width of the CTFS grows with the box until a transition phase, where a new
 350 CTFS fits in the box. For the two smaller computational boxes in the z
 351 direction ($\pi/2$ and π), only one CTFS appears (Figure 12 top and middle).
 352 Therefore, $L_R/h = 0.78$ and 1.57 for cases I and II, respectively. However,
 353 when extending the computational box to 2π in the spanwise direction, a
 354 transition phase occurs (Figure 12 bottom). Two velocity vortices and four
 355 thermal ones are perfectly visible in the left part of the channel. In the
 356 right side, the same CTFS is starting to be created, but it is still in process.
 357 A slightly wider computational box is needed in order to properly capture 2
 358 CTFS perfectly structured. This explains the differences in the statistics and
 359 the discrepancy about the width of the velocity CTFS with another works
 360 [7, 8, 15]. Accurate statistics, both for the flow and the thermal field, need
 361 wide boxes, with at least four CTFS well represented.

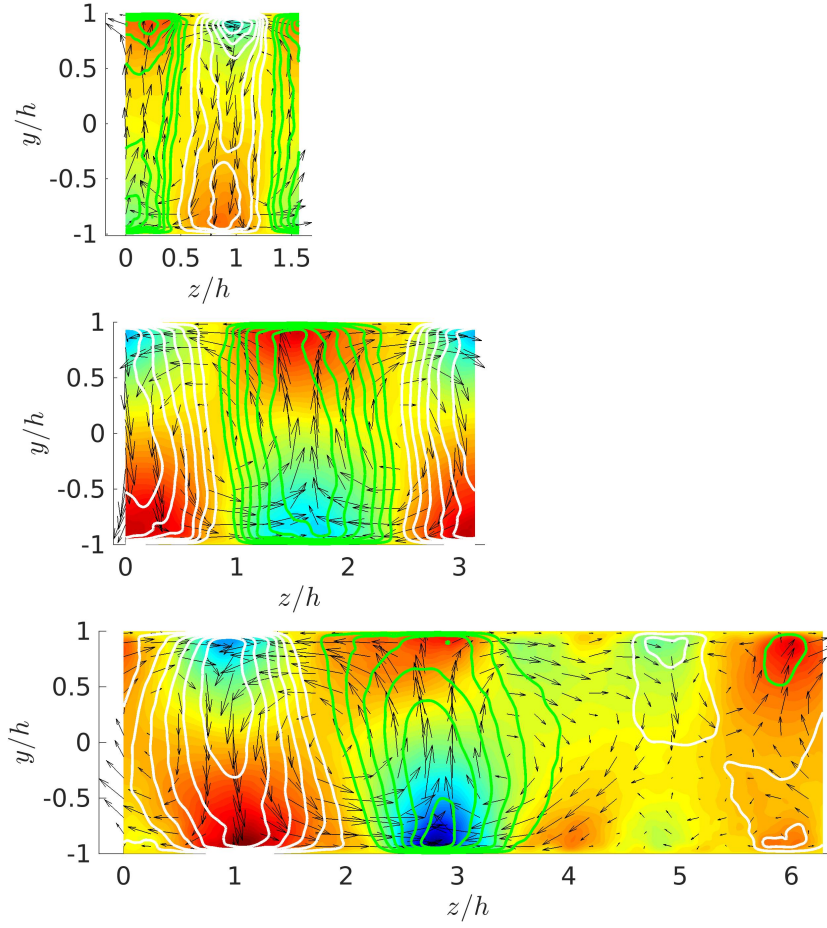


Figure 12: Colour online. Top: case I. Middle: case II. Bottom: case III. Contours of $\langle \theta \rangle_x$. White and green lines represent contours of positive and negative $\langle u \rangle_x$, respectively. $(\langle v \rangle_x, \langle w \rangle_x)$ vector field is represented by arrows.

362 4. Summary and conclusions

363 In summary, two simulations of thermal flows at larger numbers of Reynolds
364 and larger boxes than those previously simulated have been described. The
365 perturbations of the flow field present a well organized structure in form of
366 positive and negative velocity rolls. These structures leave a trace in the
367 time-averaged flow field. The superstructure made of two velocity rolls and
368 four thermal ones in the time-averaged field has been defined as a Couette
369 Thermal Flow Superstructure. This implies that unlike for the PF, there
370 seems to be less spanwise meandering of large-scale structures in the CF. In
371 this context, Abe et al. [36] also reported in the PF that when the streamwise
372 domain is reduced down to $L_x \approx 400$ at $Re_\tau = 1020$, the two-dimensional
373 behavior is established so that there is a tight coupling between the near-wall
374 and outer-layer structures. This tight coupling may also be observed in the
375 present CTFS and will be studied in future works. The CTFS presents two
376 symmetries and their size and number has been found to depend on the com-
377 putational box size. Thermal quantities appear to be not totally symmetric
378 or antisymmetric, in contrast to PFs. Using a second set of simulations at
379 $Re_\tau = 180$, it has been seen that the CTFS do not affect neither the mean ve-
380 locity nor the mean thermal flow. Moreover, mean-related quantities such as
381 the Nusselt number are also not affected. On the other hand, the width and
382 numbers of rolls, i.e. the size of the computational box, affect the value of
383 the first order statistics of the flow. This explain the small differences found
384 in the bibliography about the width of these rolls. Moreover, this makes
385 the width of the box an essential parameter to obtain accurate statistics.
386 Symmetry-based theories [39], can give an insight into why this CTFS con-

387 figuration is totally lost in Poiseuille flows. The statistics of all simulations
388 can be downloaded from the web page of our group.

389 **Acknowledgments**

390 This work was supported by the MINECO/FEDER, under project ENE2015-
391 71333-R. The computations of the new simulations were made possible by
392 a generous grant of computing time from the Barcelona Supercomputing
393 Centre, reference FI-2018-1-0037. FAA is partially funded by GVA/FEDER
394 project ACIF2018. We are very grateful for the advices and revision provided
395 by one of the referees of the article, as it has helped to enrich its content.

396 **References**

- 397 [1] J. Kim, P. Moin, and R. Moser. Turbulence statistics in fully developed
398 channels flows at low Reynolds numbers. *Journal of Fluid Mechanics*,
399 177:133–166, 1987.
- 400 [2] Sergio Hoyas and Javier Jiménez. Scaling of the velocity fluctuations in
401 turbulent channels up to $Re_\tau = 2003$. *Physics of Fluids*, 18(1):011702,
402 2006.
- 403 [3] M. Bernardini, S. Pirozzoli, and P. Orlandi. Velocity statistics in tur-
404 bulent channel flow up to $Re_\tau = 4000$. *Journal of Fluid Mechanics*,
405 758:327–343, 2014.
- 406 [4] M. Lee and R. Moser. Direct numerical simulation of turbulent channel
407 flow up to $Re_\tau \approx 5200$. *Journal of Fluid Mechanics*, 774:395–415, 2015.

- 408 [5] Yoshinobu Yamamoto and Yoshiyuki Tsuji. Numerical evidence of log-
409 arithmic regions in channel flow at $Re_\tau = 8000$. *Physical Review Fluids*,
410 3:012602(R), 2018.
- 411 [6] T. Tsukahara, H. Kawamura, and K. Shingai. Dns of turbulent cou-
412 ette flow with emphasis on the large-scale structure in the core region.
413 *Journal of Turbulence*, 7:1–16, 2006.
- 414 [7] V. Avsarkisov, S. Hoyas, M. Oberlack, and J.P. García-Galache. Turbu-
415 lent plane Couette flow at moderately high reynolds number. *Journal*
416 *of Fluid Mechanics*, 751:R1, 2014.
- 417 [8] S. Pirozzoli, M. Bernardini, and P. Orlandi. Turbulence statistics in cou-
418 ette flow at high reynolds number. *Journal of Fluid Mechanics*, 758:323–
419 343, 2014.
- 420 [9] M. Lee and R. Moser. Extreme-scale motions in turbulent plane couette
421 flows. *Journal of Fluid Mechanics*, 842:128–145, 2018.
- 422 [10] Sergio Gandía-Barberá, Sergio Hoyas, Martin Oberlack, and Stefanie
423 Kraheberger. The link between the Reynolds shear stress and the
424 large structures of turbulent Couette-Poiseuille flow. *Physics of Flu-*
425 *ids*, 30(4):041702, 2018.
- 426 [11] J. Komminaho, A. Lundbladh, and A. Johansson. Very large structures
427 in plane turbulent Couette flow. *Journal of Fluid Mechanics*, 320:259–
428 258, 1996.
- 429 [12] N. Tillmark and P.H. Aldredsson. Large scale structures in turbulent
430 plane couette flow. *Advances in Turbulence VII*, pages 59–62, 1998.

- 431 [13] O. Kitoh, K. Nakabyashi, and F. Nishimura. Experimental study on
432 mean velocity and turbulence characteristics of plane Couette flow: Low-
433 Reynolds-number effects and large longitudinal vortical structure. *Journal of Fluid Mechanics*, 539:199–227, 2005.
434
- 435 [14] O. Kitoh and M. Umeki. Experimental study on large-scale streak struc-
436 ture in the core region of turbulent plane Couette flow. *Physics of Fluids*,
437 20(2):025107, 2008.
- 438 [15] N. Tillmark. *Experiments on transition and turbulence in plane Couette*
439 *flow*. PhD thesis, KTH, Royal Institute of Technology, 1995.
- 440 [16] S. Kraheberger, S. Hoyas, and M. Oberlack. Dns of a turbulent couette
441 flow at constant wall transpiration up to $Re_\tau = 1000$. *Journal of Fluid*
442 *Mechanics*, 835:421–443, 2018.
- 443 [17] H. Kawamura, H. Abe, and K. Shingai. DNS of turbulence and heat
444 transport in a channel flow with different Reynolds and Prandtl num-
445 bers and boundary conditions. *Turbulence, Heat and Mass Transfer*
446 *3 (Proc. of the 3rd International Symposium on Turbulence, Heat and*
447 *Mass Transfer)*,, 2000.
- 448 [18] B. Debusschere and C.J. Rutland. Turbulent scalar transport mecha-
449 nisms in plane channel and couette flows. *International Journal of Heat*
450 *and Mass Transfer*, 47(8-9):1771–1781, 2004.
- 451 [19] T. Tsukahara, H. Kawamura, and K. Shingai. Dns of turbulent heat
452 transfer in plane couette flow with emphasis on the large-scale structure.
453 *Thermal Science & Engineering*, 13(4):10–11, 2005.

- 454 [20] J. Slotnick, A. Khodadoust, J. Alonso, D. Darmofal, W. Gropp, E. Lurie,
455 and D. Mavriplis. "cfd vision 2030 study: A path to revolutionary
456 computational aerosciences". *NASA TECHNICAL REPORT*, (218178),
457 2014.
- 458 [21] M. Duponcheel, L. Bricteux, M. Manconi, G. Winckelmans, and Y. Bar-
459 tosiewicz. Assessment of rans and improved near-wall modeling for
460 forced convection at low prandtl numbers based on les up to $Re_\tau = 2000$.
461 *International Journal of Heat and Mass Transfer*, 75:470–482, 2014.
- 462 [22] G. Grötzbach. Challenges in low-prandtl number heat transfer simula-
463 tion and modelling. *Nuclear Engineering and Design*, 264:41–55, 2013.
- 464 [23] S Saha, Cheng Chin, HM Blackburn, and ASH Ooi. The influence of
465 pipe length on thermal statistics computed from DNS of turbulent heat
466 transfer. *International Journal of Heat and Fluid Flow*, 32(6):1083–1097,
467 2011.
- 468 [24] Alcántara-Ávila, F. and Hoyas, S. and Pérez-Quiles, M.J. DNS of ther-
469 mal channel flow up to $Re_\tau = 2000$ for medium to low Prandtl numbers.
470 *International Journal of Heat and Mass Transfer*, 127:349–361, 2018.
- 471 [25] R. Vinuesa, C. Prus, P. Schlatter, and H.M. Nagib. Convergence of
472 numerical simulations of turbulent wall-bounded flows and mean cross-
473 flow structure of rectangular ducts. *Meccanica*, 51(12):3025–3042, 2016.
- 474 [26] A. Lozano-Durán and J. Jiménez. Effect of the computational domain
475 on direct simulations of turbulent channels up to $Re_\tau = 4200$. *Physics*
476 *of Fluids*, 26(1):011702, 2014.

- 477 [27] F. Lluesma-Rodríguez, S. Hoyas, and MJ Pérez-Quiles. Influence of the
478 computational domain on dns of turbulent heat transfer up to $Re_\tau =$
479 2000 for $Pr = 0.71$. *International Journal of Heat and Mass Transfer*,
480 122:983–992, 2018.
- 481 [28] N Kasagi, Y Tomita, and A Kuroda. Direct numerical simulation of
482 passive scalar field in a turbulent channel flow. *Journal of Heat Transfer*,
483 114(3):598–606, August 1992.
- 484 [29] S. Hoyas and J. Jiménez. Reynolds number effects on the Reynolds-
485 stress budgets in turbulent channels. *Physics of Fluids*, 20(10):101511,
486 2008.
- 487 [30] V. Avsarkisov, M. Oberlack, and S. Hoyas. New scaling laws for turbu-
488 lent Poiseuille flow with wall transpiration. *Journal of Fluid Mechanics*,
489 746:99–122, 2014.
- 490 [31] S. K. Lele. Compact finite difference schemes with spectral-like resolu-
491 tion. *Journal of Computational Physics*, 103(1):16–42, 1992.
- 492 [32] Philippe R Spalart, Robert D Moser, and Michael M Rogers. Spec-
493 tral methods for the Navier-Stokes equations with one infinite and two
494 periodic directions. *Journal of Computational Physics*, 96(2):297–324,
495 1991.
- 496 [33] Hiroyuki Abe, Robert Anthony Antonia, and Toh Sadayoshi. Large-
497 scale structures in a turbulent channel flow with a minimal streamwise
498 flow unit. *Journal of Fluid Mechanics*, 850:733–768, 2018.

- 499 [34] Hiroshi Kawamura, Kouichi Ohsaka, Hiroyuki Abe, and Kiyoshi Ya-
500 mamoto. DNS of turbulent heat transfer in channel flow with low to
501 medium-high Prandtl number fluid. *International Journal of Heat and*
502 *Fluid Flow*, 19(5):482–491, 1998.
- 503 [35] Hiroyuki Abe and Robert Anthony Antonia. Relationship between the
504 heat transfer law and the scalar dissipation function in a turbulent chan-
505 nel flow. *Journal of Fluid Mechanics*, 830:300–325, 2017.
- 506 [36] Hiroyuki Abe and Robert Anthony Antonia. Mean temperature calcu-
507 lations in a turbulent channel flow for air and mercury. *International*
508 *Journal of Heat and Mass Transfer*, 132:1152–1165, 2019.
- 509 [37] S. Hane, T. Tsukahara, and H. Kawamura. DNS of turbulent heat
510 transfer in plane Couette flow. *Proc of 13th International Heat Transfer*
511 *Conference*, August 2006.
- 512 [38] Steffen Straub, Daniel Beck, Bettina Frohnapfel, Philipp Schlatter, and
513 Ricardo Vinuesa. The effect of the selected thermal boundary conditions
514 on a fully developed turbulent pipe flow. *16th European Turbulence*
515 *Conference*, August 2017.
- 516 [39] M. Oberlack. A unified approach for symmetries in plane parallel tur-
517 bulent shear flows. *Journal of Fluid Mechanics*, 427:299–328, 2001.